Key Points:
- Height-resolved measurements of thermospheric metastable helium have been extended to an altitude of 1,000 km
- Measurements over 8 months show the seasonal progression of metastable helium density
- The metastable helium layer peaks at higher altitudes than previously thought

Correspondence to:

C. Geach,
christopher.geach@dlr.de

Author Contributions:

Conceptualization: B. Kaifler
Data curation: C. Geach
Funding acquisition: B. Kaifler
Methodology: C. Geach
Project administration: B. Kaifler
Software: C. Geach, B. Kaifler
Supervision: B. Kaifler
Visualization: C. Geach
Writing – original draft: C. Geach
Writing – review & editing: B. Kaifler

Seasonal and Altitude Dependence of Thermospheric Metastable Helium Densities Measured by Fluorescence Lidar

C. Geach[1] and B. Kaifler[2]

[1]Deutsches Zentrum für Luft- und Raumfahrt, Institut für Solar-Terrestrische Physik, Neustrelitz, Germany, [2]Deutsches Zentrum für Luft- und Raumfahrt, Institut für Physik der Atmosphäre, Oberpfaffenhofen, Germany

Abstract Airglow originating from metastable helium He(2^3S) at 1,083 nm has been used to study the upper thermosphere since its discovery in 1959, yielding insights into, for example, solar EUV intensities and thermospheric photoelectron densities. For over 6 decades, these measurements were made passively, relying on solar illumination of the He(2^3S) layer to produce a detectable signal, resulting in a column integration of the He(2^3S) layer. Recently, the first height-resolved measurements of He(2^3S) density were made by fluorescence lidar, opening a new window for studying the upper thermosphere. We report on a series of 51 measurements by this instrument spanning an entire winter season and extending to an altitude of 1,000 km, revealing a broad He(2^3S) layer that peaks at higher altitudes than previously expected.

Plain Language Summary Given the increasing number of satellites in low Earth orbit, and society's increasing reliance on these satellites, it is important to improve our understanding of the thermosphere - the layer of Earth's atmosphere in which these satellites orbit. Remote observation of this layer is challenging, due to the extremely low densities of the air at these altitudes. However, a new lidar system has been developed to study metastable helium, one constituent of the thermosphere. By tuning a powerful, pulsed laser to the absorption line of metastable helium, and collecting the scattered photons with a co-aligned telescope, altitude profiles of metastable helium density can be determined. This instrument recently made a series of 51 measurements from September 2023 to April 2024, revealing a metastable helium layer that peaks at higher altitudes than expected. These results can help refine models of our thermosphere and help pave the way for future, more powerful lidars capable of measuring temperature and wind profiles through the thermosphere.

1. Introduction

Helium is a relatively minor constituent of Earth's upper atmosphere, but it nevertheless plays an important role in thermospheric dynamics (Bernstein & Pilinski, 2022; Thayer et al., 2012). The study of thermospheric helium is limited by a lack of remote observational capabilities, but measurements of airglow at 1,083 nm, originating from helium in the upper thermosphere, offer an enticing observational window. First discovered in 1959 during a strong auroral event over Moscow (Mironov et al., 1959), the origin of the airglow was quickly identified to be the solar-induced fluorescence of metastable He(2^3S), which forms in a broad layer at altitudes above 250 km, with peak number densities of a few atoms cm^{-3} (Waldrop et al., 2005). Since Mironov et al. (1959), observations with increasing sensitivity and spatial, temporal, and spectral resolution (Christensen et al., 1971; Tinsley & Christensen, 1976; Kerr et al., 1996; Noto et al., 1998; N. N. Shefov et al., 2009) have been paired with increasingly sophisticated models of He(2^3S) production mechanisms (N. Shefov, 1961; Ferguson & Schlüter, 1962; McElroy, 1965; Bishop & Link, 1993; Waldrop et al., 2005), leading to insights into, for example, thermospheric photoelectron densities, solar EUV intensities, and thermospheric temperatures.

However, passive measurements of He(2^3S) airglow suffer from two drawbacks: (a) passive measurements are sensitive only to the column integrated brightness, meaning that derived quantities represent averages over many hundred km, and (b) passive measurements rely on solar illumination of the He(2^3S) layer, limiting the times at which observations are possible. A new tool for observations of thermospheric He(2^3S) was recently demonstrated, first by Kaifler et al. (2022) and more recently by Zhao et al. (2024): a fluorescence lidar capable of making height-resolved measurements of He(2^3S) density up to altitudes of 700 and 1,000 km, respectively. The performance of the instrument from Kaifler et al. (2022) has now been improved; here we present the latest

Table 1
Spectroscopic Properties of He Transitions Around 1,083 nm (Drake & Morton, 2007)

No.	Transition	Vac. wavelength (nm)	Oscillator strength
1	$2^3S_1 - 2^3P_2$	1,083.3,306,444	0.29948
2	$2^3S_1 - 2^3P_1$	1,083.3,216,751	0.17969
3	$2^3S_1 - 2^3P_0$	1,083.2,057,472	0.05990

observational data set, consisting of measurements of He(2^3S) densities spanning the 2023–2024 winter season and extending to an altitude of 1,000 km.

2. He(2^3S) Production, Distribution, and Fluorescence

The main production mechanism for He(2^3S) is impact of photoelectrons (with energies >19.8 eV), either locally produced or transported from the geomagnetic conjugate point, on ground state helium. Because observations are as yet only possible when the local solar zenith angle is sufficiently large (>95°, to avoid Rayleigh scattering in the lower atmosphere from contaminating the signal), the ideal observation conditions are therefore produced when the local atmosphere is still in shadow, but the conjugate point is illuminated by sunlight. As will be seen, this results in a maximum of He(2^3S) density around the winter solstice. Penning ionization effectively quenches the metastable state at altitudes below 250 km; at higher altitudes, photoionization is the primary destruction mechanism. The transition to the ground state is forbidden through single-photon processes, leading to a natural lifetime of ~7,800 s and allowing for an appreciable buildup of He(2^3S) under appropriate conditions.

He(2^3S) can be further excited to the 2^3P state, resulting in fluorescent scattering. The 2^3P state is a triplet, with wavelengths and oscillator strengths given in Table 1; at temperatures above 600 K (typical in the thermosphere), transitions 1 and 2 blend together due to thermal broadening of the absorption line. Theoretical spectra for this combined absorption line for a range of thermospheric temperatures are shown in Figure 1.

3. Observational Technique

Fluorescence lidars probing metallic constituents of the mesosphere and lower thermosphere have been used for decades to measure number densities of the respective constituents as well as temperatures and line-of-sight winds (Bowman et al., 1969; Fricke & von Zahn, 1985; She & Yu, 1994; She et al., 2002; Kawahara et al., 2017; Li et al., 2018). The idea to extend the technique into the upper thermosphere by targeting He(2^3S) was first proposed by Gerrard et al. (1997). The implementation of this idea was first attempted by Carlson et al. (2009), but the first demonstration of a helium fluorescence lidar was finally achieved by Kaifler et al. (2022), resulting in height-resolved measurements of He(2^3S) density up to an altitude of 700 km. The instrument's capabilities were then extended to make multi-frequency measurements across the He(2^3S) spectrum, leading to a proof-of-concept Doppler measurement yielding estimates of thermospheric temperatures and neutral vertical winds, albeit with large uncertainties (Kaifler & Geach, 2024). The lidar was also used to make a series of 51 measurements between September 2023 and April 2024 at the German Aerospace Center in Oberpfaffenhofen, Germany (48°N, 11°E), yielding preciser constraints of He(2^3S) density, extending to a higher altitude than the Kaifler et al. (2022) measurements, and spanning an entire measurement season (Geach & Kaifler, 2024). More details to the instrumental setup are included in Appendix A and in Kaifler et al. (2022) and Kaifler and Geach (2024).
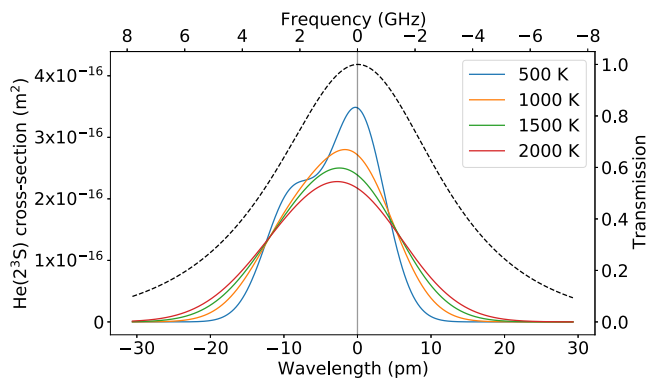
4. Analysis

Following Gerrard et al. (1997), the backscattered signal $S(\lambda, z)$ obtained by a vertically oriented lidar measuring at wavelength λ from an altitude z may be written as

$$S(\lambda) = \eta\left(\frac{P_L \tau}{E_\gamma}\right)(\rho \sigma \Delta z)\left(\frac{A}{4\pi z^2}\right) + N_B, \qquad (1)$$

where η is the end-to-end coupling efficiency of the lidar system (encompassing atmospheric transmission, beam and field of view overlap, receiver transmission, detector efficiency, etc.), P_L is the output power of the laser, τ is the integration time, E_γ is the energy per photon, $\sigma(\lambda)$ is the scattering cross-section of He(2^3S), $\rho(z)$ is the number density of He(2^3S), Δz is the altitude

Figure 1. Theoretical Doppler-broadened scattering cross-section of He(2^3S) for several temperatures. The dashed line shows the transmission spectrum of the instrument receiver, normalized to unity, and the vertical gray line shows the nominal measurement wavelength of the laser.

range, A is the receiving area of the telescope, and N_B is the altitude-independent background noise.

After subtracting the background and calibrating the instrument's response using Rayleigh scattering from the lower atmosphere, $\rho(z)$ can therefore be extracted from the backscattered signal. Further details to the filtering, background subtraction and calibration can be found in Appendix B and in Kaifler and Geach (2024).

5. Results and Discussion

5.1. Altitude Profiles

Figure 2 shows the monthly mean profiles of morning He(2^3S) number density, binned by solar zenith angle (SZA). The measurements are shown up to an altitude of 980 km (Sep.-Dec. 2023 measurements) and 1,000 km (Jan.-Apr. measurements); data from higher altitudes are available, but they are excluded due to the increasing uncertainties with altitude. Nevertheless, the profiles as shown demonstrate a broad He(2^3S) layer, with a peak density occurring at higher altitudes compared to what has been previously predicted (Bishop & Link, 1999; Tinsley & Christensen, 1976; Waldrop et al., 2005). As pointed out by Rundel and Stebbings (1974), such a He(2^3S) layer could be due to high thermospheric temperatures associated with the current solar maximum, which would cause the thermosphere to expand upwards and increase the production rate of He(2^3S). Indeed, the December profiles shown in Figure 2 match well to the calculated results corresponding to a thermospheric temperature of 1500 K in Figure 4 of Rundel and Stebbings (1974). This is also consistent with the multi-frequency measurements made with the instrument described here (Kaifler & Geach, 2024), from which temperatures of 1260 K (1σ confidence interval: 830–1790 K) or 2230 K (1σ confidence interval: 1360–3580 K) were derived, depending on the choice of analysis technique.

The measurements reported in Kaifler et al. (2022) extended to an altitude of 700 km and as such were unable to measure the peak of the He(2^3S) layer; in these measurements, on the other hand, a clear peak is often visible—for example, in the December profile for SZAs between 110° and 130°. As the measurements progress toward sunrise, the overall He(2^3S) density increases, but the increase is larger at higher altitudes; in the measurements closest to sunrise, with SZAs between 100° and 95°, the peak is no longer clear, indicative of a He(2^3S) layer that extends to even higher altitudes. This is presumably a consequence of the thermosphere warming under solar illumination. Note that the peak is not always present or clearly discernible, for example at SZAs greater than 130° or in the months at the beginning or end of the measurement campaign - this is due to decreased signal-to-noise at those times, due primarily to decreased He(2^3S) densities.

Also of note is the presence of He(2^3S) in the December and January profiles for SZAs greater than 130°. Though the densities are low, they are consistently positive, and neither shows signs of having peaked below 1,000 km. The presence of He(2^3S) at these SZAs is a promising sign for future helium lidar measurements, especially as the performance of the instrument improves, as it significantly increases the time during which measurements are possible. However, Waldrop et al. (2005) suggest that at such large SZAs, the production of He(2^3S) from recombination of He$^+$ becomes significant. González and Sulzer (1996) additionally demonstrate that the He$^+$ layer forms at the H$^+$/O$^+$ transition altitude; production of He(2^3S) from recombination of He$^+$ could therefore explain the large apparent vertical extent of the He(2^3S) layer at these times, given the increase in the H$^+$/O$^+$ transition height during increased solar activity (Kutiev et al., 1994). Thus, there could in principle be two sub-populations of He(2^3S), each with its own characteristic temperature and wind speed. Given sufficient signal-to-noise, a retrieval of both neutral He and He$^+$ temperatures would be possible, but such a retrieval would require measurements at a minimum of 6 wavelengths across the He(2^3S) fluorescence line to adequately constrain the spectrum.

The January He(2^3S) densities shown here are higher by a factor of $\sim$2 relative to those shown in Kaifler et al. (2022). This could be due in part to an increase in solar activity as the next solar maximum approaches, but a more likely explanation is pulse overlap in the 2022 measurements. The 200 Hz repetition rate used at that time corresponds to a pulse separation of 750 km, meaning that He(2^3S) returns from altitudes between 850 and 1,000 km were attributed to the range-independent background estimated between 100 and 250 km. This presumably led to an over-estimation of the background, and a corresponding under-estimation of the He(2^3S) density.
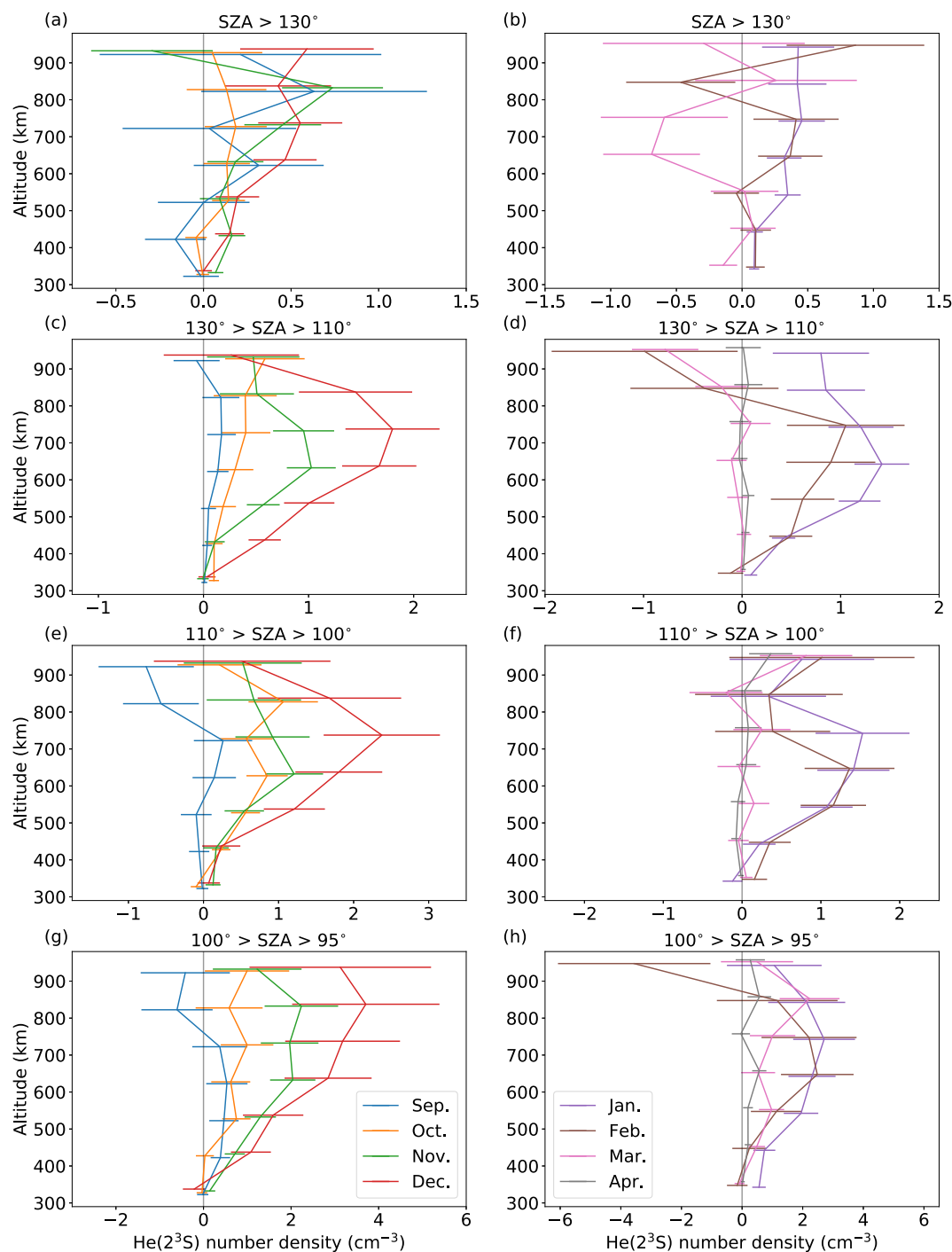
Figure 2. Monthly mean profiles of He(2^3S) number density from Sep.-Dec. 2023 (left column) and from Jan.-Apr. 2024 (right column). As in Kaifler et al. (2022), the data were binned by solar zenith angle (SZA): >130° (a, b), 130°-110° (c, d), 110°-100° (e, f), and 100°-95° (g, h). Note that the data points are displaced by up to ±8 km vertically to increase readability.

An exciting prospect offered by these measurements is the possibility to retrieve the underlying He(1^1S) density profiles. Waldrop et al. (2005) used models of the photoelectron flux and He(1^1S) densities to calculate He(2^3S) production rates and densities, but this process could be run in the other direction: using models of photoelectron flux and sufficiently precise measurement of He(2^3S) densities, height- and time-resolved estimates of He(1^1S) densities could be inferred, at least for times when the production of He(2^3S) is dominated by photoelectron impact.
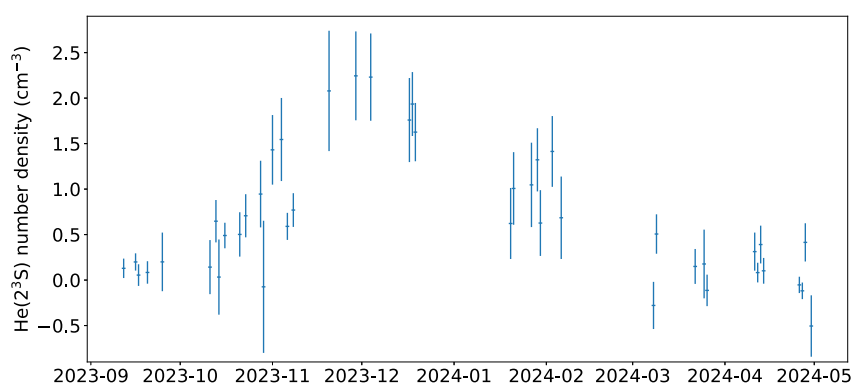
Figure 3. Time series of He(2^3S) number density measurements, averaged over an altitude range from 500 to 800 km and over solar zenith angles from 95° to 130°.

5.2. Seasonal Dependence

To track the seasonal variation in He(2^3S) density, we analyzed each measurement independently, averaging over an altitude range from 500 to 800 km and integrating over solar zenith angles from 95° to 130°. We omitted measurements with less than 30 min integration time after all filters were applied; the resulting 43 measurements are shown in Figure 3. As expected, He(2^3S) density peaks near the winter solstice, due in part to the increased density of ground state helium in winter (Liu et al., 2014) and in part to the increased supply of photoelectrons from the geomagnetic conjugate point. Attempts to retrieve winds and temperatures via lidar returns are therefore most feasible in the period from early November to mid-February, though this measurement season varies with location, depending on solar illumination locally and at the geomagnetic conjugate point.

One peculiarity of the time series shown in Figure 3 is that much of the short-term variability (few days) may be attributed to instrument noise: with only few exceptions, the uncertainty interval of each data point overlaps with the uncertainty intervals of the previous and following measurement. The variability in He(2^3S) density must therefore be smaller than the typical measurement error and may be as small as 20%–30%. However, one should also note that the measurements were all taken at roughly the same local time, and any potential variability due to the effect of solar tides and resulting changes in the circulation is thus suppressed.

6. Conclusion

The helium fluorescence lidar operating at the German Aerospace Center has been extended to make He(2^3S) number density measurements up to an altitude of 1,000 km, and a series of 51 measurements spanning an entire winter season has been made. Though the seasonal progression of He(2^3S) density matches well to previous predictions, the measurements reveal a He(2^3S) layer that peaks at higher altitudes than previously expected.

Future plans for the helium fluorescence lidar include replacing the telescope mirror and detector to improve system performance by ∼2 orders of magnitude, enabling higher precision measurements of He(2^3S) density with higher temporal and vertical resolution. As demonstrated in Kaifler and Geach (2024), such an instrument will also be able to place height- and time-resolved constraints on thermospheric temperatures and neutral winds. Thus, the helium fluorescence lidar will continue a long history of using He(2^3S) as window into remote observation of the thermosphere.

Appendix A: Instrument Technical Details

Section 3 includes a general description of the instrument used to make the measurements presented here, but many technical details of the instrumental setup and operation were omitted; these are included here.

The helium fluorescence lidar consists of a Q-switched Nd : GdVO$_4$ laser, a fiber-coupled telescope with a diameter of 762 mm and a field of view of 61 μrad, an optical filter consisting of a coarse 0.7 nm interference filter and two narrow-band, air-gapped etalons (with a combined bandwidth of 29.7 nm), and a custom-made super-conducting nanowire single-photon detector from Quantum Opus with ∼30% detection efficiency and ∼70 Hz

dark counts. Two mechanical choppers have been installed: one in the receiver, to block backscatter from the lower 15 km of the atmosphere and prevent saturation of the detector, and one in the laser to prevent potential afterglow of the laser from contaminating the measurement. Otherwise the instrument is as described in Kaifler et al. (2022).

The instrument was operated in various modes over the 2023–2024 measurement campaign: (a) From September–December 2023, the laser wavelength was tuned to the maximum of the He(2^3S) backscatter spectrum ($\lambda = 1{,}083.3306$ nm, vacuum) and had an effective pulse repetition rate of 75 Hz, corresponding to a measurement range of 2,000 km. Due to practical considerations, the laser was in fact operated with a pulse repetition rate of 150 Hz, but the wheel of the laser chopper was adapted to block every other pulse. Since the mechanical chopper in the receiver was synchronized to the laser, it also blocked light from entering the receiver halfway between consecutive emitted pulses, corresponding to altitudes from 980 to 1,015 km in the reconstructed profiles. (b) In January and February 2024, the laser was operated in a multi-frequency mode, with measurements at four wavelengths across the He(2^3S) spectrum in order to derive temperature and line-of-sight wind estimates (Kaifler & Geach, 2024). Here we include only measurements made at the wavelength corresponding to the He(2^3S) backscatter maximum, which account for ∼20% of the total. During the multi-frequency measurements, the laser was operated with a pulse repetition rate of 115 Hz, corresponding to a measurement range of 1,300 km. (c) In March and April 2024, the laser was again tuned to the maximum of the He(2^3S) backscatter spectrum, but the pulse repetition rate remained at 115 Hz.

Appendix B: Analysis Technical Details

Section 4 gave a short overview of the process from which number densities of He(2^3S) can be extracted from the raw lidar data; here, we present further details to the analysis process, particularly the background estimation, instrumental calibration, and uncertainty analysis.

The total uncertainty on the measurements has three principal components: measurement photon noise on the measurements themselves, uncertainty due to background subtraction, and uncertainty on the conversion factor by which we convert the received lidar signal into He(2^3S) densities. The photon noise is simply estimated as the square root of the received signal within a given time and altitude bin. A more thorough treatment of the analysis and uncertainty estimate calculation is given in Kaifler et al. (2022); here, we describe differences in the present analysis relative to that work.

In order to estimate the altitude-independent background, an altitude range must be identified where no laser-synchronous signals are present. In Kaifler et al. (2022), the background was estimated at altitudes between 100 and 250 km; at these altitudes, Rayleigh scattering is negligible and no He(2^3S) is present due to Penning ionization. For the measurements presented here that were made with a 75 Hz repetition rate, the background is estimated at altitudes from 1,500 to 1,950 km, providing tighter constraints on the background estimates due to a longer integration time. At these higher altitudes, it is unlikely that significant He(2^3S) is present, and any trace He(2^3S) remaining will contribute negligibly to our detected signal, given the $1/z^2$ factor for backscatter signals. We were not able to exclude the possibility that He(2^3S) is present above 1,000 km; therefore, for the measurements made with a 115 Hz repetition rate, we estimate the background using the 100–250 km altitude range.

As in Kaifler et al. (2022), this background noise estimate was subtracted from the data. The return signals were then calibrated based on the Rayleigh returns between 36 and 50 km to account for variations in laser power and atmospheric transmission. The mechanical chopper blocked light from the bottom 15 km of the atmosphere; therefore, no filtering based on the presence of clouds was possible. This contaminated our estimates of solar-induced He(2^3S) fluorescence but introduced no bias into our retrieved He(2^3S) densities. Measurement periods in which clouds were present resulted in attenuated Rayleigh and fluorescence signals, and the calibration of the measurements by the Rayleigh returns compensated for this variation. Periods in which thick cloud cover occurred were excluded due to the resulting low signal levels.

An additional effect that was neglected in Kaifler et al. (2022) is the differential receiver transmission for return signals originating from Rayleigh scattering and from fluorescent scattering, due to the difference in wavelengths between those two sources. The magnitude of this effect depends on the temperature and winds at the He(2^3S) layer, as well as on the transmission curve of the receiver. Due to a slow leak in one of the receiver etalons, the

transmission curve drifted by up to 0.5 p.m. per day, though the receiver was periodically re-tuned such that the total drift was never more than 10 p.m. from its nominal position (dashed black line in Figure 1). Correcting for this effect is particularly important for spectral measurements reported on in Kaifler and Geach (2024) and is discussed in more detail there. Here, we calculated this correction factor for thermospheric temperatures between 700 and 1500 K, thermospheric winds between −50 m/s and 50 m/s, and etalon drifts up to 10 p.m. Taking the mean and standard deviation of the correction factor across this parameter space gives 1.12 ± 0.05. The He(2^3S) densities reported above were scaled by this result, and standard error propagation was used to compute the contribution from this correction to the reported uncertainties.

He(2^3S) densities were calculated based on an assumed scattering cross-section of 2.78×10^{-16} m², corresponding to a thermospheric temperature of 1000 K with no vertical wind. Uncertainty on this value, given the same assumed temperature and wind parameter space as above, results in a further 11% contribution to the calculated He(2^3S) densities.

Finally, the telescope was focused at 600 km in order to maximize the backscatter from the He(2^3S) layer. This results in sub-optimal coupling of backscatter originating from altitudes between 36 and 50 km, where the Rayleigh signal was measured. To compensate for this effect, we scale the Rayleigh signal by a factor of 1.06 ± 0.02, where the uncertainty comes from uncertainty in the location of the telescope focus, which drifted with temperature and needed to be periodically corrected. See the supplement of Kaifler and Kaifler (2021) for details on computing the coupling efficiency. Optimum overlap between the laser beam and the telescope field of view was maintained by using the conical scan method, also described in that paper.

Data Availability Statement

Data used in this paper have been made available at https://zenodo.org/records/13838346 (Geach & Kaifler, 2024).

References

Bernstein, V., & Pilinski, M. (2022). Drag coefficient constraints for space weather observations in the upper thermosphere. *Space Weather*, *20*(5), e2021SW002977. https://doi.org/10.1029/2021SW002977

Bishop, J., & Link, R. (1993). Metastable He 1083 nm intensities in the twilight: A reconsideration. *Geophysical Research Letters*, *20*(11), 1027–1030. https://doi.org/10.1029/93gl01117

Bishop, J., & Link, R. (1999). He(23 s) densities in the upper thermosphere: Updates in modeling capabilities and comparisons with midlatitude observations. *Journal of Geophysical Research*, *104*(A8), 17157–17172. https://doi.org/10.1029/1999JA900151

Bowman, M. R., Gibson, A. J., & Sandford, M. C. W. (1969). Atmospheric sodium measured by a tuned laser radar. *Nature*, *221*(5179), 456–457. https://doi.org/10.1038/221456a0

Carlson, C. G., Dragic, P. D., Kirk Price, R., Coleman, J. J., & Swenson, G. R. (2009). A narrow-linewidth, YB fiber-amplifier-based upper atmospheric Doppler temperature lidar. *IEEE Journal of Selected Topics in Quantum Electronics*, *15*(2), 451–461. https://doi.org/10.1109/JSTQE.2009.2012403

Christensen, A. B., Patterson, T. N., & Tinsley, B. A. (1971). Observations and computations of twilight helium 10,830-Ångstrom emission. *Journal of Geophysical Research*, *76*(7), 1764–1777. https://doi.org/10.1029/ja076i007p01764

Drake, G. W. F., & Morton, D. C. (2007). A multiplet table for neutral helium (4he i) with transition rates. *The Astrophysical Journal - Supplement Series*, *170*(1), 251–260. https://doi.org/10.1086/512239

Ferguson, E. E., & Schlüter, H. (1962). Metastable helium atom concentrations in the earth's atmosphere. *Planetary and Space Science*, *9*(10), 701–710. https://doi.org/10.1016/0032-0633(62)90127-7

Fricke, K., & von Zahn, U. (1985). Mesopause temperatures derived from probing the hyperfine structure of the D2 resonance line of sodium by lidar. *Journal of Atmospheric and Terrestrial Physics*, *47*(5), 499–512. https://doi.org/10.1016/0021-9169(85)90116-3

Geach, C., & Kaifler, B. (2024). Helix 2023-2024 measurement campaign [Dataset]. https://doi.org/10.5281/zenodo.13838346

Gerrard, A. J., Kane, T. J., Meisel, D. D., Thayer, J. P., & Kerr, R. B. (1997). Investigation of a resonance lidar for measurement of thermospheric metastable helium. *Journal of Atmospheric and Solar-Terrestrial Physics*, *59*(16), 2023–2035. https://doi.org/10.1016/S1364-6826(97)00046-1

González, S. A., & Sulzer, M. P. (1996). Detection of he+ layering in the topside ionosphere over Arecibo during equinox solar minimum conditions. *Geophysical Research Letters*, *23*(18), 2509–2512. https://doi.org/10.1029/96GL02212

Kaifler, B., & Geach, C. (2024). Proof of concept demonstration of a metastable helium fluorescence lidar for thermospheric wind and temperature measurements. *Optics Letters*, *49*(15), 4437–4440. https://doi.org/10.1364/OL.528925

Kaifler, B., Geach, C., Büdenbender, H. C., Mezger, A., & Rapp, M. (2022). Measurements of metastable helium in earth's atmosphere by resonance lidar. *Nature Communications*, *13*(1), 6042. https://doi.org/10.1038/s41467-022-33751-6

Kaifler, B., & Kaifler, N. (2021). A compact Rayleigh autonomous lidar (CORAL) for the middle atmosphere. *Atmospheric Measurement Techniques*, *14*(2), 1715–1732. https://doi.org/10.5194/amt-14-1715-2021

Kawahara, T. D., Nozawa, S., Saito, N., Kawabata, T., Tsuda, T. T., & Wada, S. (2017). Sodium temperature/wind lidar based on laser-diode-pumped Nd:YAG lasers deployed at Tromsø, Norway (69.6{ }\textdegreeN, 19.2{ }\textdegreeE). *Optics Express*, *25*(12), A491–A501. https://doi.org/10.1364/OE.25.00A491

Kerr, R. B., Noto, J., Lancaster, R. S., Franco, M., Rudy, R. J., Williams, R., & Hecht, J. H. (1996). Fabry perot observations of helium 10830 Å emission at millstone hill. *Geophysical Research Letters*, *23*(22), 3239–3242. https://doi.org/10.1029/96gl03052

Kutiev, I., Stankov, S., & Marinov, P. (1994). Analytical expression of o+/h+ ion transition surface for use in iri. *Advances in Space Research*, *14*(12), 135–138. https://doi.org/10.1016/0273-1177(94)90254-2

Li, T., Ban, C., Fang, X., Li, J., Wu, Z., Feng, W., et al. (2018). Climatology of mesopause region nocturnal temperature, zonal wind and sodium density observed by sodium lidar over Hefei, china (32{}\textdegree n, 117{}\textdegree e). *Atmospheric Chemistry and Physics*, *18*(16), 11683–11695. https://doi.org/10.5194/acp-18-11683-2018

Liu, X., Wang, W., Thayer, J. P., Burns, A., Sutton, E., Solomon, S. C., et al. (2014). The winter helium bulge revisited. *Geophysical Research Letters*, *41*(19), 6603–6609. https://doi.org/10.1002/2014GL061471

McElroy, M. B. (1965). Excitation of atmospheric helium. *Planetary and Space Science*, *13*(5), 403–433. https://doi.org/10.1016/0032-0633(65)90032-2

Mironov, A. V., Prokudina, V. S., & Shefov, N. N. (1959). Observation of the aurora over Moscow on February 10-11, 1958 (in Russian). In *Spectral, Electrophotometrical, and Radar Studies of Aurorae and Airglow* (pp. 20–24).

Noto, J., Kerr, R. B., Shea, E. M., Waldrop, L. S., Fisher, G., Rudy, R. J., et al. (1998). Evidence for recombination as a significant source of metastable helium. *Journal of Geophysical Research*, *103*(A6), 11595–11603. https://doi.org/10.1029/97ja03062

Rundel, R. D., & Stebbings, R. F. (1974). Metastable helium in the Earth's upper atmosphere. *Journal of Geophysical Research*, *79*(4), 681–684. https://doi.org/10.1029/ja079i004p00681

She, C. Y., Vance, J. D., Williams, B. P., Krueger, D. A., Moosmüller, H., Gibson-Wilde, D., & Fritts, D. (2002). Lidar studies of atmospheric dynamics near polar mesopause. *Eos, Transactions American Geophysical Union*, *83*(27), 289–293. https://doi.org/10.1029/2002EO000206

She, C. Y., & Yu, J. R. (1994). Simultaneous three-frequency Na lidar measurements of radial wind and temperature in the mesopause region. *Geophysical Research Letters*, *21*(17), 1771–1774. https://doi.org/10.1029/94GL01417

Shefov, N. (1961). On the nature of helium emission 10830 Å in aurorae. *Planetary and Space Science*, *5*(1), 75–76. https://doi.org/10.1016/0032-0633(61)90044-7

Shefov, N. N., Semenov, A. I., & Yurchenko, O. T. (2009). Empirical model of variations in the helium 1083 nm emission: 1. Intensity. *Geomagnetism and Aeronomy*, *49*(1), 93–103. https://doi.org/10.1134/s0016793209010137

Thayer, J. P., Liu, X., Lei, J., Pilinski, M., & Burns, A. G. (2012). The impact of helium on thermosphere mass density response to geomagnetic activity during the recent solar minimum. *Journal of Geophysical Research*, *117*(A7). https://doi.org/10.1029/2012JA017832

Tinsley, B. A., & Christensen, A. B. (1976). Twilight helium 10,830-Å calculations and observations. *Journal of Geophysical Research*, *81*(7), 1253–1263. https://doi.org/10.1029/ja081i007p01253

Waldrop, L. S., Kerr, R. B., González, S. A., Sulzer, M. P., Noto, J., & Kamalabadi, F. (2005). Generation of metastable helium and the 1083 nm emission in the upper thermosphere. *Journal of Geophysical Research*, *110*(A8). https://doi.org/10.1029/2004JA010855

Zhao, R., Liu, Z., Xue, X., Zhou, H., Wang, Z., Liu, Y., et al. (2024). Metastable helium lidar for thermosphere and lower exosphere measurements: Instrument description and initial results. *Space Weather*, *22*(8), e2024SW003977. https://doi.org/10.1029/2024SW003977